

Element-selective magnetometry in ferrimagnetic erbium iron garnetC. Strohm,^{*} T. Roth, C. Detlefs, P. van der Linden, and O. Mathon
European Synchrotron Radiation Facility, BP220, 38043 Grenoble, France

(Received 1 July 2012; revised manuscript received 23 November 2012; published 20 December 2012)

The emergence of a field induced canted phase below a critical temperature is one of the characteristic properties of ferrimagnets with two inequivalent antiferromagnetically coupled sublattices. Using x-ray magnetic circular dichroism at the Fe *K* edge, we have performed element selective magnetometry in ferrimagnetic erbium iron garnet in fields up to 30 T. The signal from the tetrahedral Fe sites at 70 K allows the detection of the two transitions at 10 and 23 T bounding the canted phase and the direct observation of the reversal of the Fe-sublattice magnetization within this phase.

DOI: [10.1103/PhysRevB.86.214421](https://doi.org/10.1103/PhysRevB.86.214421)

PACS number(s): 75.50.Gg, 75.25.-j, 75.30.Kz

I. INTRODUCTION

When Forestier and Guiot-Guillain reported the synthesis of a new class of compounds from mixtures of iron (Fe_2O_3) and rare-earth (R_2O_3) oxides,¹ the magnetic properties of these compounds immediately raised interest. The correct interpretation of the intriguing magnetization curves² led Bertaut and Forrat to identify and isolate a new series of pure ferrites with a structure isotype to the garnet minerals³ from these compounds: $\text{R}_3\text{Fe}_2\text{Fe}_3\text{O}_{12}$ (RIG), where R is a heavy rare earth (Sm-Lu) and where the iron occupies two sites of different symmetry. The cubic unit cell (space group: $Ia\bar{3}d$, #230) contains eight formula units, in each of which three Fe occupy sites of tetrahedral symmetry (*d*), two Fe occupy sites of octahedral coordination (*a*), and three R are located at the center of distorted cubes (*c*). The dominant coupling between the different cations is due to ferrimagnetic superexchange interactions over the oxygen anions, whose strength is determined by the bond distances and angles. The interaction between the *a* and *d* Fe sites is strongest, and the ferrimagnetic alignment ($\uparrow_d \uparrow_d \uparrow_d \downarrow_a \downarrow_a$) with a net moment of about $5\mu_B$ per formula unit is only broken at the Curie temperature of 560 K or in extremely high magnetic fields. The interaction between the two Fe and the R sublattices is smaller by one order of magnitude, and the R-R interaction is smaller by two orders of magnitude. Given this hierarchy of interactions ($\text{Fe}_d\text{-Fe}_a \gg \text{Fe}_{\text{net}}\text{-R} \gg \text{R-R}$), the system's behavior at low temperature and moderate magnetic fields can be adequately reproduced by an effective two-sublattice approximation, where R behaves as a paramagnet which is antiferromagnetically coupled to the net moment Fe_{net} of the iron sites.⁴ One of the remarkable properties of the two-sublattice ferrimagnets is the emergence of a canted phase below a critical temperature T_{crit} . If the saturation magnetization of the R sublattices exceeds that of the Fe sublattices, this phase extends to zero field, leading to a compensation temperature T_{comp} , where a large polarization of each sublattice goes along with a vanishing external magnetization (see Fig. 1).

The RIGs were at the heart of the demonstration of the local molecular-field theory, and, in his Nobel lecture, Néel considered that “the best illustration of ferrimagnetism is undoubtedly provided by iron garnets.”⁵ Since then, in particular, the mixed garnets have found various applications ranging historically from bubble memories over microwave devices to optical insulators, while the pure RIGs remain still of

fundamental interest. Many studies on the latter were devoted to the exploration of the magnetic phase diagrams.^{4,6–12} The observation of the entire field dependence of their sublattice magnetizations remains, however, a formidable challenge today, because of the large applied fields required to reach saturation. The recent development of synchrotron x-ray techniques for the element-^{13,14} and isotope-selective¹⁵ study of magnetic properties in high magnetic fields has opened new possibilities in this field.

For this study, we have combined Fe *K*-edge x-ray magnetic circular dichroism (XMCD)¹⁶ with magnetic fields up to 30 T, which are sufficient to compete with the local molecular fields in $\text{Er}_3\text{Fe}_5\text{O}_{12}$ (ErIG) and to reach all phases characteristic of the interaction of the two sublattices. The field dependence below the compensation point allows one to observe the two second-order transitions bounding the canted phase and to quantitatively follow the reversal of the Fe-sublattice magnetization in the canted phase. By comparison with a simple model, we show that the XMCD amplitude at the pre-edge directly probes the net magnetization of the Fe sublattices.

The field was applied along the crystallographic (100) direction, for which the phase diagram was previously studied up to very high fields in Ref. 11. Figure 1 shows a simulation of the phase diagram for a two-sublattice ferrimagnet assuming a simple isotropic model developed in the general introduction to “Neel Ferrimagnets” by Clark and Callen.⁴ Even though complications due to crystal-field effects⁶ are expected at low temperatures, the model allows one to appreciate the basic underlying physics. For the orientation, temperature, and field range under study here, the model agrees with Ref. 11 and the XMCD data of the present experiment. For the model, we use the theoretical saturation magnetizations of $5\mu_B$ for the Fe sublattice and $27\mu_B$ for the Er sublattice. The dimensionless molecular-field constant, being the only free parameter, was adjusted to $\lambda = 26.5$, in order to reproduce T_{comp} and the measured bulk magnetization data at a constant field (\circ) shown in Fig. 3(a).

II. EXPERIMENT

The experiments were performed at the energy dispersive x-ray-absorption and XMCD beamline ID24 at the European Synchrotron Radiation Facility.¹⁷ In the optical scheme of the

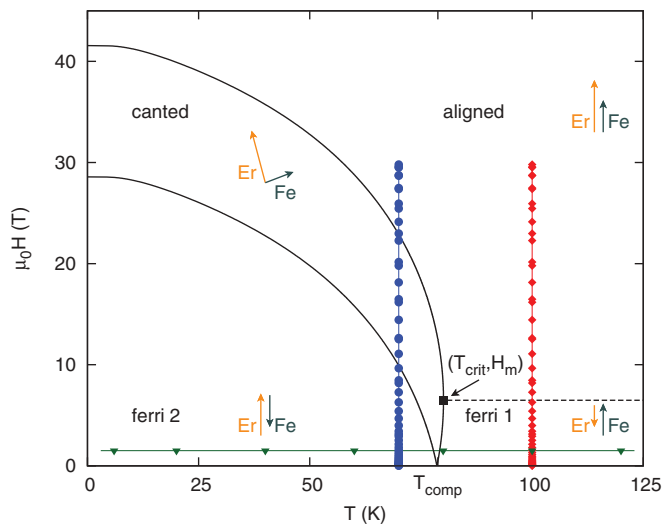


FIG. 1. (Color online) Simulation of the magnetic phase diagram of $\text{Er}_3\text{Fe}_5\text{O}_{12}$ for fields applied along the (100) direction using an isotropic two-sublattice model. Solid black lines show the lower and upper boundaries of the canted phase, respectively. The dashed black line shows the field at which the Er sublattice is completely demagnetized. Colored points and lines represent the locations of the XMCD spectra and calculated magnetization curves shown in Figs. 2 and 3. (\blacktriangledown) denotes temperature dependence at 1.5 T, (\bullet) denotes field dependence at 70 K, and (\blacklozenge) denotes field dependence at 100 K.

energy dispersive setup, a bent silicon crystal, illuminated by a divergent beam, focuses the latter onto the sample position and introduces at the same time a correlation between the direction of propagation and the photon energy. This energy-angle correlation is in turn used to map the full transmission spectrum on a fast position sensitive detector. The absence of any moving parts and the simultaneous acquisition of the energy spectra offer distinct advantages for differential techniques like XMCD and time-resolved applications, as, for example, experiments in pulsed fields. The light of circular polarization is generated using a diamond (111) quarter wave plate in a quasi-non-dispersive setting with the Si (111) polychromator crystal. The XMCD signal was acquired at fixed polarization while flipping the magnetic field according to the procedure detailed in Ref. 18. As the maximum continuous fields available for XMCD are currently bound to 17 T by the limits of affordable superconducting magnet technology, we use a miniature pulsed magnet system¹⁹ combined with time-resolved detection schemes^{13,20} to reach fields that are high enough to compete with the molecular fields, to explore the magnetic phase diagram of the RIGs. The sample was cut from a single crystal, oriented to ± 2 deg along the (100) direction and mechanically polished to a thin platelet. A piece of about 1 mm² was sandwiched between two Si substrates with laser drilled holes, in order to obtain a free standing sample in the focal spot of the beam. The thickness was estimated to 28 μm from the observed average edge jump of 2.

XMCD at the Fe K edge has been measured many times before in the RIGs,^{21–25} but with a different focus, as, for example, angular²¹ and compositional dependencies,^{22–24} and was treated theoretically in Refs. 26 and 27. The objective of the present study is to use Fe K -edge XMCD to directly

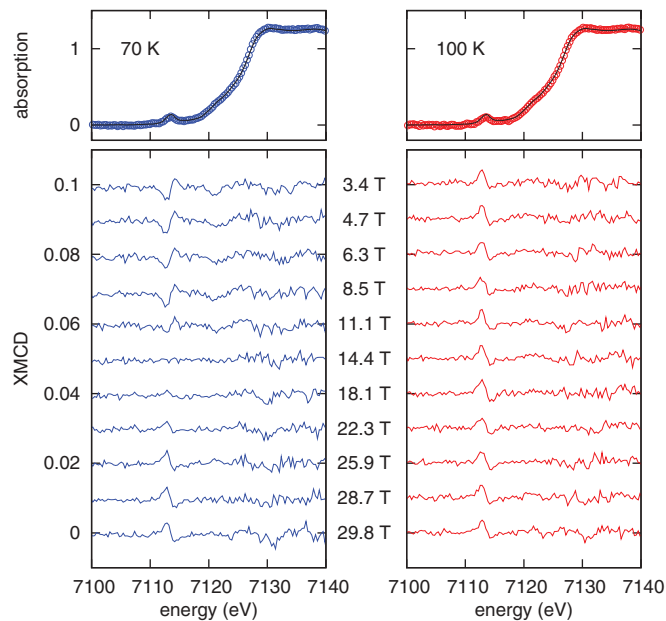


FIG. 2. (Color online) XAS and XMCD in $\text{Er}_3\text{Fe}_5\text{O}_{12}$ above and below the compensation point. Top: normalized absorption spectra. Points show data taken at ID24. Lines show the reference spectrum for the energy calibration recorded at BM29. Bottom: selected XMCD spectra. Data for different field values are offset for clarity.

observe the Fe-sublattice magnetization M_{Fe} along different cuts through the phase diagram. In order to cover all ordered phases that are characteristic for a two-sublattice ferrimagnet, we measured a temperature dependence at low field across the compensation point $T_{\text{comp}} = 78.8$ K, one field dependence below and one above the compensation point. The points reported in Fig. 1 represent the location of the actual data points in the phase diagram.

The temperature dependence (green triangles) was recorded at the maximum of the field pulse adjusted to 1.5 T, similar to Ref. 13, whereas the field dependencies were acquired using a multiframe detection scheme,²⁰ which is at the origin of the irregular spacing of the points. Figure 2 shows selected energy spectra for the magnetic-field dependence at 70 K (blue dots) and at 100 K (red diamonds). The absorption spectra (points) at the top were normalized to an edge jump of 1. The reference spectra (lines) that were used for the energy calibration of the position sensitive detector are reproduced for comparison. The marked prepeak arises mainly from the tetrahedral d sites.^{26,27} The XMCD spectra shown in the lower part of Fig. 2 exhibit strong derivative-shape features at the pre-edge, whereas no significant XMCD signal is observed at the main edge with the available statistics. The amplitude of the first lobe is slightly higher than the second. These observations are in agreement with previous measurements on ErIG ²⁴ and other RIGs.²⁵ A number of qualitative observations can directly be made on the spectra in Fig. 2: At low field (3.4 T), the XMCD signal changes sign when crossing T_{comp} . Above T_{comp} , at 100 K there is no visible change in the spectra up to the highest fields. Below T_{comp} , at 70 K, in the first four spectra (3.4–8.5 T) there is no change, then the amplitude starts to decrease, vanishes at 14.4 T, rises again with opposite sign, and finally remains constant throughout the last three spectra (25.9–29.8 T).

III. RESULTS AND DISCUSSION

For a quantitative interpretation, the XMCD amplitude was evaluated as the difference between the extrema at 7112.9 and 7114.2 keV. Figure 3 shows the XMCD amplitude (right scale) together with calculations for the sublattice magnetizations (left scale) using the isotropic two-sublattice model. We use the same relative scaling for the XMCD and magnetization

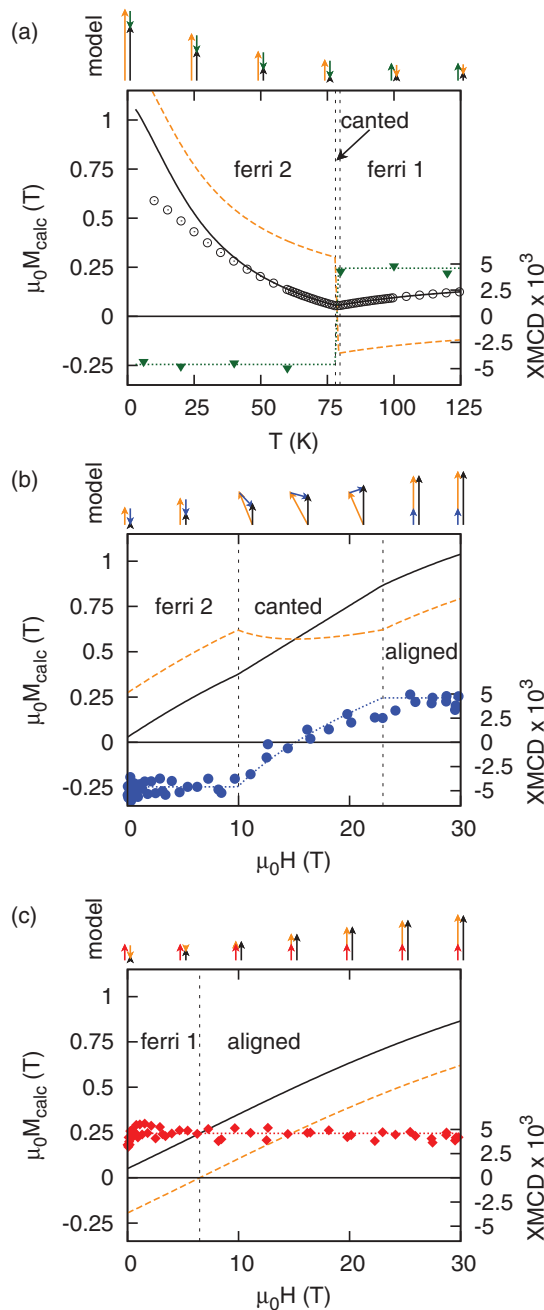


FIG. 3. (Color online) Fe K -edge XMCD amplitude ($\blacktriangledown, \bullet, \blacklozenge$) and calculated total (solid line), Fe-sublattice (dotted line), and Er-sublattice (dashed line) magnetizations in $\text{Er}_3\text{Fe}_5\text{O}_{12}$. (a) Temperature dependence at 1.5 T, where (c) denotes the measured bulk magnetization along (110). (b) Field dependence below T_{comp} at 70 K. (c) Field dependence above T_{comp} at 100 K. Arrows on top of the graphs show models of the spin configurations.

in all graphs. The solid lines show the calculated total magnetization M_{tot} of the sample as it would be observed in bulk magnetization measurements. The dashed lines represent the projection of the rare-earth-sublattice magnetization M_{zR} , and the dotted lines represent the projection of the net Fe-sublattice magnetization $M_{z\text{Fe}}$ on the applied field. The arrows on top of the graphs depict the model spin configurations at selected temperature and field values. The colored lines and points in Fig. 1 correspond to the locations of these calculations and measurements in the phase diagram.

Figure 3(a) shows the temperature dependence of the sublattice magnetizations. The net Fe moment is saturated over the whole temperature range due to the strong antiferromagnetic interaction between d and a sites. M_{zR} is opposite to $M_{z\text{Fe}}$ due to the dominating antiferromagnetic interaction between the c and d sites. At high temperature, M_R is lower than M_{Fe} and $M_{z\text{Fe}}$ is aligned with the applied field. As the temperature is lowered, M_R increases according to a Brillouin law, where the applied field is offset by the molecular field from the Fe sites. At $T_{\text{comp}} = 78.8$ K, M_R equals M_{Fe} , and, below T_{comp} , M_{zR} is aligned with the applied field. The temperature evolution of M_R is at the origin of the characteristic minimum in M_{tot} .

Figure 3(b) shows the field dependence of the sublattice magnetizations below T_{comp} . As a function of field, M_R and M_{Fe} are first opposite and $M_{z\text{Fe}}$ remains constant, while M_R follows a Brillouin function where the molecular field $H_m = \lambda M_{\text{Fe}}$ adds to the applied field. At applied fields higher than the lower critical field $H_l = \lambda |M_R - M_{\text{Fe}}|$, a canted sublattice configuration becomes energetically more favorable. Within the canted phase, the net moment of the Fe sublattice rotates by 180° , leading to the observed behavior in $M_{z\text{Fe}}$, whereas the Er moments cant slightly away, in order to let the Fe spins pass, which leads to the minimum in M_{zR} in the canted phase. Above the upper critical field $H_u = \lambda(M_R + M_{\text{Fe}})$, both sublattices are ferromagnetically aligned. The temperature dependencies of the second-order transitions bounding the canted phase are shown as solid lines in Fig. 1. These data best match the calculated sublattice magnetization and phase diagram (Fig. 1) at $T = 70$ K. The sample cryostat, however, was operated at 65 K. We attribute this difference to beam heating.

Figure 3(c) shows the field dependence of the sublattice magnetizations above T_{comp} . $M_{z\text{Fe}}$ does not evolve at all until the antiferromagnetic interaction between the a and d sites is broken at fields higher than those applied in the present experiment. The field dependence of M_{zR} is that of a paramagnet, where the applied field is reduced by the molecular field $H_m = \lambda M_{\text{Fe}}$ of the net Fe moment. In consequence, the R sublattice becomes completely demagnetized when the applied field equals the molecular field, which is indicated by the dashed line meeting the border of the canted phase at the critical temperature $T_{\text{crit}} = 80.1$ K in Fig. 1.

It is interesting to compare our measurements on the RIGs with the case of ferrimagnetic rare-earth (R) transition-metal (T) intermetallic compounds (RTI), for which very detailed studies were performed.^{28,29} For the RTIs, a sizable cross-talk was observed at both the T K edges and the R $L_{2,3}$ edges; i.e., the T K -edge XMCD contains spectral features related to the R site magnetization²⁸ and, inversely, the R $L_{2,3}$ edges reflect the behavior of the T sites.²⁹ This striking observation was explained by the indirect nature of the XMCD signal at these

edges combined with exchange interaction pathways. There are important differences between the exchange interactions in the RTIs and the RIGs, however. The ferrimagnetic exchange in the RTIs is mediated by the R $5d$ band, which is directly addressed by the L -edge XMCD, whereas the ferrimagnetic superexchange in the RIGs involves the $2p$ states of the oxygen anions. Nevertheless, an induced signal from the Fe sites was observed at the R L edges in the RIGs in Ref. 30 too, which we could confirm (Strohm, unpublished results). One might thus also expect to see an induced signal at Fe K -edge XMCD: first, because of the reciprocity of the interaction and, second, because of the role the oxygen $2p$ states play both in the superexchange and in mixing the Fe $3d$ states with the $4p$ states which are probed in Fe K -edge XMCD.^{26,27} If there was a sizable contribution in the K -edge spectra of the RIGs, we would have observed it: in the field dependence at 100 K, $M_{z\text{Fe}}$ does not evolve whereas M_{zR} changes from -0.19 to 0.62 T. In the canted phase at 70 K, on the other hand, $M_{z\text{Fe}}$ inverts from -0.24 to 0.24 T while M_{zR} varies only by 8%. In our data, there is no sign of such an induced signal within the statistical accuracy of our data. One may argue that the statistics of our data is not sufficient to discern this contribution. In the case of the RTIs, the induced R contribution at the T K edge is, however, large. A tentative explanation may be that the induced signal at the R L edges in RIGs arises mainly from the a sites, whereas in this experiment we only observe the pre-edge signal, which is mainly originated by the d sites. This would explain the absence of any induced signal in our Fe K -edge data. Future studies on the issue are expected to yield new information about XMCD spectroscopy at T K edges and R L edges itself, as well as on the ferrimagnetic exchange interactions in the RIGs.

IV. SUMMARY AND CONCLUSIONS

In conclusion, we have studied the temperature and field dependence of the Fe-sublattice magnetization in ErIG above and below T_{comp} using XMCD at the Fe K edge. In the temperature dependence, we observe the reversal of M_{Fe} at T_{comp} . At 100 K, above T_c , M_{Fe} remains constant up to the highest fields. As a function of field at 70 K, below T_{comp} , M_{Fe} first remains opposite to the applied field up to 10 T, then diminishes, reverses, and saturates again above 23 T. The temperature and field dependence of the XMCD amplitude at the pre-edge are in excellent agreement with a calculation of M_{Fe} in a simple isotropic two-sublattice model. This shows experimentally that the XMCD amplitude at the pre-edge provides a direct probe for the Fe-sublattice magnetization despite the complicated origin of the signal. With the available resolution, we did not resolve a possible contribution originated by M_R at the Fe K edge, even though the inverse is the case.³⁰ XMCD studies of the field dependence at the Er $L_{2,3}$ edges to elucidate this question are underway. It would be worth performing Fe K -edge XMCD in ErIG along the (111) direction, in order to study the effect of anisotropy inducing a first-order transition within the canted phase that was observed at low temperatures.¹¹

ACKNOWLEDGMENTS

The authors would like to thank M. Krisch for providing the crystals of $\text{Er}_3\text{Fe}_5\text{O}_{12}$ and E. Lorenzo, D. Maillard, and the Institut Néel for the bulk magnetization measurements. We further would like to thank Quantum Detectors for support with the “Ultra system” fast position sensitive detector. We acknowledge the attribution of beam time under Proposal No. HE 3347 by the European Synchrotron Radiation Facility.

*cornelius.strohm@esrf.fr

- ¹H. Forestier and G. Guiot-Guillain, C. R. Seances Acad. Sci. A **230**, 1844 (1950).
- ²R. Pauthenet, *Ann. Phys.* **3**, 424 (1958).
- ³F. Bertaut and F. Forrat, C. R. Seances Acad. Sci. A **242**, 382 (1956).
- ⁴A. E. Clark and E. Callen, *J. Appl. Phys.* **39**, 5972 (1968).
- ⁵L. Néel, *Science* **174**, 985 (1971).
- ⁶R. Alben, *Phys. Rev. B* **2**, 2767 (1970).
- ⁷G. Fillion and G. Hug, C. R. Seances Acad. Sci. B **271**, 1045 (1970).
- ⁸J. L. Féron, G. Fillion, and G. Hug, *Z. Angew. Phys.* **32**, 219 (1971).
- ⁹J. L. Féron, G. Fillion, J. Chaussy, A. Berton, and G. Hug, *Solid State Commun.* **10**, 641 (1972).
- ¹⁰J. L. Féron, G. Fillion, and G. Hug, *J. Phys.* **34**, 247 (1973).
- ¹¹K. Nakao, T. Goto, and N. Miura, *J. Magn. Magn. Mater.* **54–57**, 1363 (1986).
- ¹²M. Lahoubi, A. Bouguerra, A. Kihal, and G. Fillion, *J. Alloys Compd.* **275**, 598 (1998).
- ¹³O. Mathon, P. van der Linden, T. Neisius, M. Sikora, J. M. Michalik, C. Ponchut, J. M. De Teresa, and S. Pascarelli, *J. Synchrotron Radiat.* **14**, 409 (2007).
- ¹⁴Y. H. Matsuda, Z. W. Ouyang, H. Nojiri, T. Inami, K. Ohwada, M. Suzuki, N. Kawamura, A. Mitsuda, and H. Wada, *Phys. Rev. Lett.* **103**, 046402 (2009).

- ¹⁵C. Strohm, P. Van der Linden, and R. Rüffer, *Phys. Rev. Lett.* **104**, 087601 (2010).
- ¹⁶G. Schütz, W. Wagner, W. Wilhelm, P. Kienle, R. Zeller, R. Frahm, and G. Materlik, *Phys. Rev. Lett.* **58**, 737 (1987).
- ¹⁷S. Pascarelli, O. Mathon, M. Munoz, T. Mairs, and J. Susini, *J. Synchrotron Radiat.* **13**, 351 (2006).
- ¹⁸O. Mathon, F. Baudalet, J. P. Itié, S. Pasternak, A. Polian, and S. Pascarelli, *J. Synchrotron Radiat.* **11**, 423 (2004).
- ¹⁹P. J. E. M. van der Linden, O. Mathon, C. Strohm, and M. Sikora, *Rev. Sci. Instrum.* **79**, 075104 (2008).
- ²⁰C. Strohm, F. Perrin, M. C. Dominguez, J. Headspith, P. van der Linden, and O. Mathon, *J. Synchrotron Radiat.* **18**, 224 (2011).
- ²¹H. Yamazaki, H. Maruyama, K. Kobayashi, and K. Shimomi, *Jpn. J. Appl. Phys.* **32**, 317 (1993).
- ²²H. Maruyama, I. Harada, K. Kobayashi, and H. Yamazaki, *Physica B* **208**, 760 (1995).
- ²³N. Kawamura, H. Maruyama, K. Kobayashi, I. Inoue, and H. Yamazaki, *J. Phys. IV* **7**, 269 (1997).
- ²⁴H. Maruyama and N. Kawamura, *J. Electron Spectrosc. Relat. Phenom.* **136**, 135 (2004).
- ²⁵A. Rogalev, J. Goulon, F. Wilhelm, C. Brouder, A. Yaresko, J. BenYoussef, and M. V. Indenbom, *J. Magn. Magn. Mater.* **321**, 3945 (2009).

- ²⁶I. Harada and A. Kotani, *J. Phys. Soc. Jpn.* **63**, 1285 (1994).
- ²⁷I. Harada, T. Suzuki, and A. Kotani, *J. Phys. Soc. Jpn.* **65**, 3016 (1996).
- ²⁸M. A. Laguna-Marco, C. Piquer, and J. Chaboy, *Phys. Rev. B* **80**, 144419 (2009).
- ²⁹M. A. Laguna-Marco, J. Chaboy, C. Piquer, H. Maruyama, N. Ishimatsu, N. Kawamura, M. Takagaki, and M. Suzuki, *Phys. Rev. B* **72**, 052412 (2005).
- ³⁰N. Kawamura, M. Suzuki, H. Maruyama, and T. Ishikawa, *J. Synchrotron Radiat.* **8**, 425 (2001).